DOI: 10.13009/EUCASS2022-6075
9TH EUROPEAN CONFERENCE FOR AERONAUTICS AND SPACE SCIENCES (EUCASS)

REST HF-10 test case: Flame response to externally excitation of a methane driven rocket combustion chamber

Ansgar Lechtenberg[⋆†] *and Peter Gerlinger*[⋆]
[⋆]*German Aerospace Center (DLR)*
Institute of Combustion Technology, Numerical Simulation Department
Pfaffenwaldring 38–40, 70569 Stuttgart, Germany
Ansgar.Lechtenberg@dlr.de · Peter.Gerlinger@dlr.de
[†]Corresponding author

Abstract

In this paper, transcritical combustion of methane with oxygen is investigated numerically for a self excited and an externally excited academic test case. Thereby, the influence of excitation on flame propagation is investigated. Hybrid improved Delayed Detached Eddy Simulations (iDDES) are performed using a high order spatial discretization. Combustion is modeled by a 70-step 17-species finite-rate reaction mechanism, where subgrid fluctuations are considered by a multivariate assumed Probability Density Function (aPDF) method. Based on these numerical techniques a profound analysis of the Large-Eddy Simulation (LES) data is performed. The influence of excitation on the pressure frequency spectra is investigated as well as its impact on local extinction, taking part in some regions of the combustor.

1. Introduction

In rocket combustors enormous amounts of energy are converted. Therefore, small disturbances can potentially grow very fast. Such combustion chamber instabilities are still a major problem in the development of new propulsion systems. The consequences reach from irregular thrust to total failure of the combustor. In the history of rocket engine development, every innovation had to be tested experimentally, with the risk of losing the engine. Nowadays, accurate Computational Fluid Dynamics (CFD) simulation can reduce these risks.

Kerosene (RP-1) and hydrogen are the most frequently used fuels combined with Liquid Oxygen (LOx) as oxidizer in liquid-propellant rockets. Recently, methane came into focus as a promising rocket fuel. Kerosene is easier to handle and has a higher volumetric energy density than hydrogen. In contrast, hydrogen has a higher gravimetric energy density and a higher specific impulse. Methane combines the advantages of both, although is not as powerful as hydrogen. Nevertheless, it is easier to operate. Further, CH_4 can be extracted from biogas as a sustainable fuel and potentially synthesized on Mars, what perhaps facilitates return missions from Mars. Rocket engines powered by liquid methane/ liquid oxygen are for example the Raptor engine from SpaceX and the M10 rocket engine from Avio.

Points of interest in the simulation of rocket combustors are thermal loads, mean flame lengths, wall heat fluxes and the dynamic pressure loads. The last point requires time accurate, highly resolved simulations. The in-house code Turbulent All Speed Combusiont Multigrid Solver 3D[29] (TASCOM3D) is distinguished by high spatial order using structured grids and is used for all simulations in this paper. The main turbulent structures in the core flow are resolved in this work by the hybrid improved Delayed Detached Eddy Simulation[28] (iDDES) method. For combustion finite-rate chemistry is used and transport equations for 17 species are solved. These methods are described in more detail in Sec. 2.

The solver TASCOM3D has been validated using a large number of different test cases, both in subsonic and supersonic flows, as well as for real and ideal equation of state.[6,14,17,18,23,24,29] With respect to fuel, hydrogen and methane combustion have been investigated. In this paper, TASCOM3D is used to simulate the combustion of methane and oxygen with transcritical injection conditions similar to real rocket engine applications. Moreover, the combustion chamber is externally excited to investigate the impact of oscillations on flame propagation. Because the presented test case, which is described in detail in Sec. 3, is a purely numerical application, validation with experimental data is yet not possible. Instead, the fine resolved data is used to analyze the methane-oxygen combustion processes at high pressure.

DOI: 10.13009/EUCASS2022-6075

2. Numerical Methodology

TASCOM3D solves the filtered conservation equations of mass, momentum, energy, turbulence modeling and species transport[1,7,10,15]

$$\frac{\partial \boldsymbol{Q}}{\partial t} + \frac{\partial(\boldsymbol{F}-\boldsymbol{F_v})}{\partial x} + \frac{\partial(\boldsymbol{G}-\boldsymbol{G_v})}{\partial y} + \frac{\partial(\boldsymbol{H}-\boldsymbol{H_v})}{\partial z} = \boldsymbol{S} , \tag{1}$$

using the conservative variable vector

$$\boldsymbol{Q} = (\rho,\ \rho u,\ \rho v,\ \rho w,\ \rho E,\ \rho k,\ \rho\omega,\ \rho\sigma_T,\ \rho\sigma_Y,\ \rho, Y_i)^T \tag{2}$$

in a fully coupled way. $\boldsymbol{Q}$ consists of the density ρ, the three velocities components u,v and w, the total specific Energy E, the turbulence quantities k and ω, the temperature variance σ_T and the sum of the variance of all species mass fractions σ_Y as well as the $N_S - 1$ independent species mass fractions Y_i, where N_S is the number of species considered. Further, $\boldsymbol{F}$, $\boldsymbol{G}$ and $\boldsymbol{H}$ denote convective fluxes in each coordinate direction and $\boldsymbol{F_v}$, $\boldsymbol{G_v}$ and $\boldsymbol{H_v}$ their viscous counterparts, respectively. The source vector is given by

$$\boldsymbol{S} = (0,\ 0,\ 0,\ 0,\ 0,\ S_k,\ S_\omega,\ S_{\sigma_T},\ S_{\sigma_Y},\ S_{Y_i})^T , \tag{3}$$

including source terms of the turbulence and chemistry models. As the injector condition of the investigated test case are in the real gas regime, the Soave-Redlich-Kwong[30] (SRK) equation

$$p = \frac{R_u T}{V_m - b} - \frac{\alpha(T)}{V_m(V_m + b)} \tag{4}$$

is used to describe the thermodynamic relation. Here, R_u denotes the universal gas constant and V_m is the molecular volume which can not be neglected for high density flows.[22] Further, $\alpha(T)$ is a temperature and mixture dependent quantity, while b is a mixture dependent constant.[22]

In order to describe the chemical processes taking place finite-rate chemistry is used. The forward reaction rates of all reactions are calculated by the modified Arrhenius equation[16]

$$k_f = A\, T^n \exp\left(-\frac{E_A}{R_u T}\right) , \tag{5}$$

with the Arrhenius constant A, the temperature exponent n and the activation energy E_A. The backward reaction rates are obtained from

$$k_b = -\frac{k_f}{K_{cr}} , \tag{6}$$

where K_{cr} is the equilibrium constant. The influence of the subgrid turbulence on chemistry is considered by a multivariate assumed Probability Density Function[1,7] (aPDF) method. Here, temperature fluctuations are modeled using a Gaussian distribution, species fluctuation by a multivariate β-PDF.[11]

Spatial discretization is done on structured grids using a high order schemes. In the present investigation a 5$^{\text{th}}$ order upwind biased discretization stencil is employed To avoid numerical oscillations a Multi-Dimensional Limiting Process-Low Dissipation[8] (MLP$^{\text{ld}}$) method is used. The inviscid fluxes at cell interfaces are calculated using a member of the Advection Upstream Splitting Method[19] (AUSM) family, the Simple Low-dissipation AUSM[25] (SLAU) scheme, which has proven to achieve low numerical dissipation. The viscous fluxes are discretized with a 2$^{\text{nd}}$ order central scheme. Time discretization is done by the fully implicit Backward Differentiation Formula[5] (BDF), implemented in TASCOM3D up to third order. The obtained set of equations is efficiently solved by a Lower-Upper Symmetric Gauß-Seidel[26,27] (LU-SGS) scheme. Moreover, for the present low Mach number rocket combustor flows, an all Mach number preconditioning[36] is used.

As neither Direct Numerical Simulation (DNS) nor wall resolved Large-Eddy Simulation (LES) are feasible for high Reynolds number flows,[20] turbulence is modeled by the hybrid iDDES method. Here, the core flow is treated as LES, while in the near wall regions the Unsteady Reynolds-Averaged Navier-Stokes (URANS) equations are solved using the $k-\omega$ turbulence model of Wilcox.[34] The transition between URANS and LES is done automatically depending on mesh size, wall distance and the flow field. Thus allows efficient and reliable, time accurate simulations while resolving most of the turbulence in the rocket combustion chamber.

DOI: 10.13009/EUCASS2022-6075

Table 1: Injector dimensions and injection conditions.

	D_i (mm)	D_o (mm)	T (K)	$\dot{m}$ (kg/s)
oxidizer O_2	—	6.3	100.0	0.46
fuel CH_4	7.2	8.2	231.0	0.136

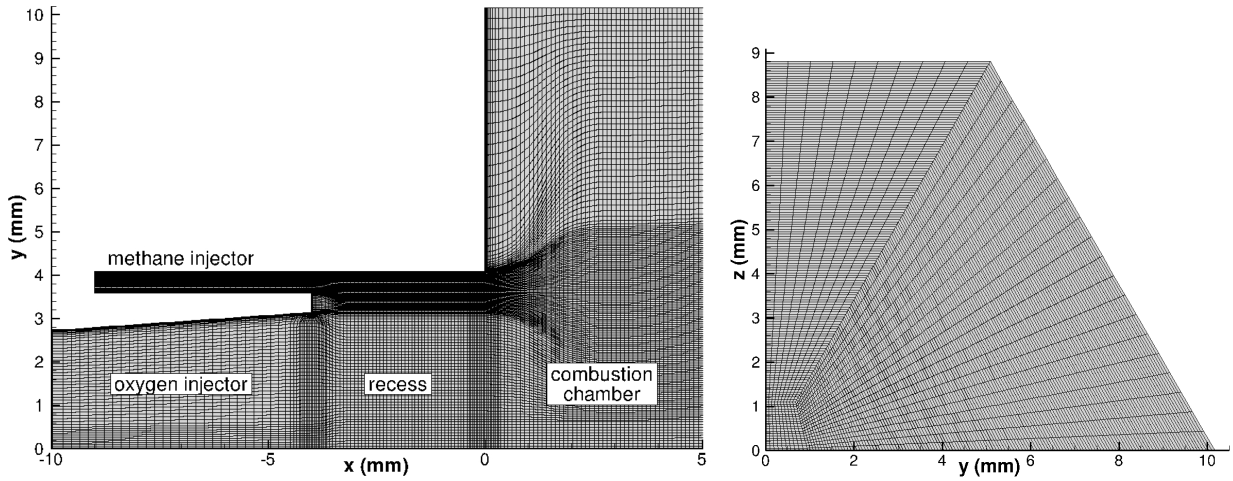

Figure 1: Computational grid for the near injector regime (left) and for a cross section at $x = 20$ mm (right).

3. Test case description and numerical setup

The investigated test case is designed to compare numerical solvers with different degrees of modeling complexity and accuracy. The combustion chamber with a length of 300 mm has a hexagonal cross section with an edge length of 10.17 mm. The face plate is modeled as an adiabatic wall. Opposing outer faces of the chamber are connected periodically to mimic a multi injector combustor. Because no nozzle is considered, the outflow is subsonic and the mean chamber pressure of 100 bar has to be prescribed by a non-reflective outflow boundary condition. The injection element consists of a co-axial injector with a recess of 4 mm length which is described by Traxinger[32] in detail. Diameters, mass flow rates and injection temperatures of the co-axial injector are given in Tab. 1 for both fuel and oxidizer. Due to the low injection temperatures, the combustor operates in transcritical regime. In order to prescribe a mean turbulent inflow profile for the injector pipes, the velocity at the inflow boundary condition is calculated using the 1/7 power law[2] with

$$u(r) = u_{max}\left(1 - \frac{r}{R}\right)^n , \quad \text{with} \quad u_{max} = \frac{(n+1)(n+2)}{2}\, u_{mean} \quad \text{and} \quad n = \frac{1}{7} . \tag{7}$$

Two test cases are investigated with the same mean mass flow rate. While the first one is without externally excitation, the oxidizer mass flow rate of the second test case is sinusoidally excited with a frequency of 5 kHz and an amplitude of 10 % of the mean mass flow rate

$$\dot{m}(t) = (1 + 0.1 \sin(2\pi f t))\ \dot{m}_{mean} . \tag{8}$$

For both test cases, time averaging of simulation data is performed over 10 ms, which corresponds to 50 cycles for the excited test case. With respect to the mean velocity inside the combustor ($\sim$ 150 m/s) this is equivalent to five flow through times, which is considered to be sufficient for convergence. Further, symmetry is used for spatial averaging.

As mentioned above, TASCOM3D is based on structured grids. For two different planes, the mesh is depicted in Fig. 1. It consists of 12.2 million volumes and is significantly refined towards the walls to resolve the boundary layers of the injector head accurately (Fig. 1, left). Thereby, a dimensionless wall distance of $y^+ < 10$ is achieved. To check if the grid resolution is sufficient for LES, two different criteria are used: The amount of resolved turbulent kinetic energy γ and the capability to reproduce the turbulent energy cascade. For the former,, γ can be written as[3]

$$\gamma = \frac{k_{res}}{k_{tot}} , \quad \text{with} \quad k_{res} = 0.5(\widetilde{u''^2} + \widetilde{v''^2} + \widetilde{w''^2}) \quad \text{and} \quad k_{tot} = k_{res} + k_{mod} . \tag{9}$$

Both, the variances of the velocities $\widetilde{u''^2}$, $\widetilde{v''^2}$, $\widetilde{w''^2}$ and the mean modeled turbulent kinetic energy k_{mod} are calculated during runtime. Davidson[3] assumes a grid to be well resolved, if $\gamma > 80\,\%$. As depicted in Fig. 2, the amount of

DOI: 10.13009/EUCASS2022-6075

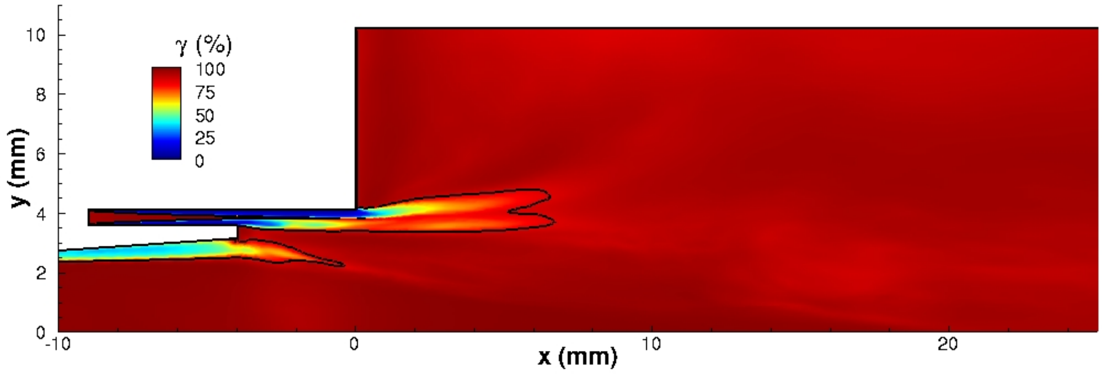

Figure 2: Amount of resolved turbulent kinetic energy γ at the injector head. Black isoline for $\gamma = 85\,\%$.

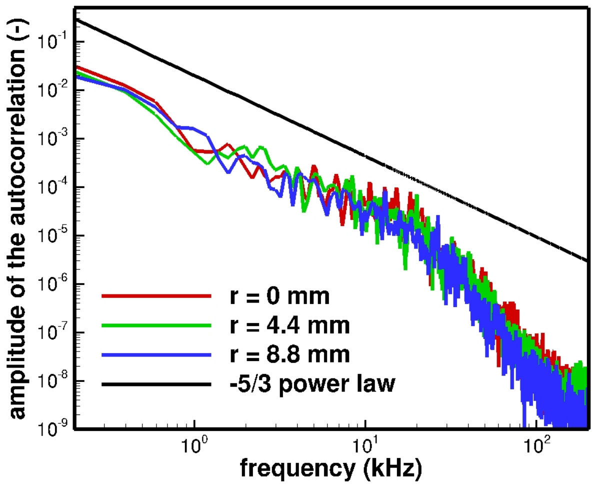

Figure 3: FFT of the energy of the axial velocity component at $x = 100\,\text{mm}$ for different radial positions r. Kolmogorov's $-5/3$ power law line as reference.

resolved turbulent kinetic energy is mostly higher than 85 % except of small parts in the shear layers. This is due to the transition from URANS mode inside the injector pipes to LES mode inside the combustion chamber and is a well known drawback of hybrid iDDES schemes.[28]

To show, that the simulation correctly reproduces the turbulent energy cascade, the autocorrelation of the axial velocity for the discrete time signal

$$\Psi(x, t_0 + n\Delta t) = \frac{\sum_{m=0}^{N/2}(u_m - \overline{u})(u_{m+n} - \overline{u})}{\sum_{m=0}^{N/2}(u_m - \overline{u})(u_m - \overline{u})}\ , \quad \text{with} \quad u_i = u(x, t_0 + i\Delta t) \quad \text{for} \quad n = 0 \cdots N/2 \tag{10}$$

as described by Pope[20] is performed for monitor points at $x = 100\,\text{mm}$ and different radial positions. Here, N is the total amount of recorded time steps. The spatial dimension of the eddies is interpreted here as local temporal fluctuation correlated with the mean velocity $\overline{u}$. This is justified due to Taylor's hypothesis.[31] The Fast Fourier Transformation (FFT) of the autocorrelation transforms the time signal into its frequency domain and is displayed in Fig. 3. For all three points it can be seen, that the simulated frequency spectra follow the -5/3 power law over more than one decade in both frequency and amplitude. According to Frölich[4] this indicates a sufficient grid resolution of LES. Thus, two different criteria confirm the mesh resolution to be reasonable.

DOI: 10.13009/EUCASS2022-6075

4. Results and Discussion

4.1 Averaged and instantaneous flow fields

In order to give an overview of the mean flow field, Figs. 4 and 5 depict the mean distributions of several quantities in different planes. The isoline of the stoichiometric mixture fraction is used to indicate the mean flame extension (Fig. 4, top). It is calculated according to Bilger and Warnatz[33] by

$$\xi_i = \frac{Z_i - Z_{i,ox}}{Z_{i,fuel} - Z_{i,ox}} \ , \quad \text{with} \quad Z_i = \sum_j^{N_{Sp}} \mu_{i,j} Y_j \ . \tag{11}$$

Here, $\mu_{i,j}$ is the element mass fraction of element i in species j. The subscripts 'fuel' and 'ox' denote quantities at the fuel and oxidizer inlets, respectively. Because ξ_i is equal for each element, the mixture fraction can be simplified be written for the element carbon as

$$\xi = \xi_{\mathrm{C}} = \frac{Z_{\mathrm{C}}}{Z_{C,fuel}} \ , \quad \text{with} \quad Z_{C,ox} = 0 \quad \text{and} \quad Z_{C,fuel} = \mu_{C,\mathrm{CH_4}} \ . \tag{12}$$

The global reaction of the combustion of methane with oxygen

$$\mathrm{CH_4} + 2\mathrm{O_2} \rightarrow \mathrm{CO_2} + 2\mathrm{H_2O} \tag{13}$$

results in a stoichiometric mixture fraction $\xi_{stoich} = 0.2$.

Independent from the excitation, the mean flame length is almost identical for both simulations (114 mm for the self excited test case and 120 mm for the externally excited test case) and the mean temperature distributions vary only slightly. As can be seen in the temperature distributions (Fig. 4, top), the mean flow composition changes from cold educts to hot products between $x = 50$ mm and $x = 150$ mm. Thereby, the density decreases strongly and causes an acceleration of the flow. The increase of the velocity is associated with a decrease in mean pressure (Fig. 4, bottom), which drops by 4.5 bar in the combustor. 75 % of the pressure decrease occurs within the range $x = 50$ to 150 mm. Fig. 4 also depicts the recirculation zones close to the face plate. The mean flow field attaches to the periodic boundaries at $x \approx 14$ mm. Thereby, the flow recirculates not only perpendicular to the main axis (Fig. 4) but also tangential to the periodic boundary (Fig. 5).

Likewise, the instantaneous temperature distributions in Fig. 6 show a similar behavior for both operation points. In the first part of the combustor the flame is thin and strongly folded. At $x \approx 120$ mm the dense LOx core desintegrates and hot gas distributes over the entire cross section. Furthermore, burned fluid crosses the periodic boundaries which indicates flame interaction. In accordance with the mean temperature distributions (Fig. 4, top) the instantaneous fields confirm that the combustion is almost completed in the last third of the combustor.

Close to the injectors flame extinction occurs as can bee seen in Fig. 7. Initially, the flame is smooth and attached to the injector tip. As shear layer instabilities grow, the flame is stretched by the emerging vortices. This process is highlighted in Fig. 7 on the left hand side by white circles. Fig. 7 shows the same structures on the right hand side advanced in time by about 50 µs. Here one can clearly observe the flame extinction in the white circles as the hot flame is interrupted by a cold zone. In these volumes, for both fuel and oxidizer the mixture fraction is $Y_{Ox,fuel} > 0.1$. Hence, they are present in considerable quantities and are mixed but not combusted. Such events of local flame extinction happen more frequently and slightly further upstream for the excited test case, which may explain the somewhat longer mean flame length observed above.

The growth of the shear layer instabilities is visualized for the same time steps in the bottom part of Fig. 7 by the Q-criterion.[13] Directly at the injector, regions of high vorticity are limited to the outer shear layer between fuel and surrounding recirculated gas. Due to the high density gradients perpendicular to the hot flame region, the growth of the instabilities in the inner shear layer is reduced. Cause is the pseudo boiling of the oxygen, as investigations of cold trans- and supercritical nitrogen jets confirm.[21] Thus, in the inner shear layer regions with high Q-values start to occur a few millimeter further downstream than for the outer shear layer. With increasing homogenization of the velocity field further downstream the vorticity decreases. Furthermore, the flame reignites again and no flame extinction can be observed downstream of $x \approx 60$ mm. This is investigated in more detail in Sec. 4.3.

4.2 Behavior of the dynamic pressure

Concerning pressure oscillations there are significant differences between simulations with nozzle and this test case, where the nozzle is not considered. The longitudinal modes depend directly on the length of the combustion chamber.

DOI: 10.13009/EUCASS2022-6075

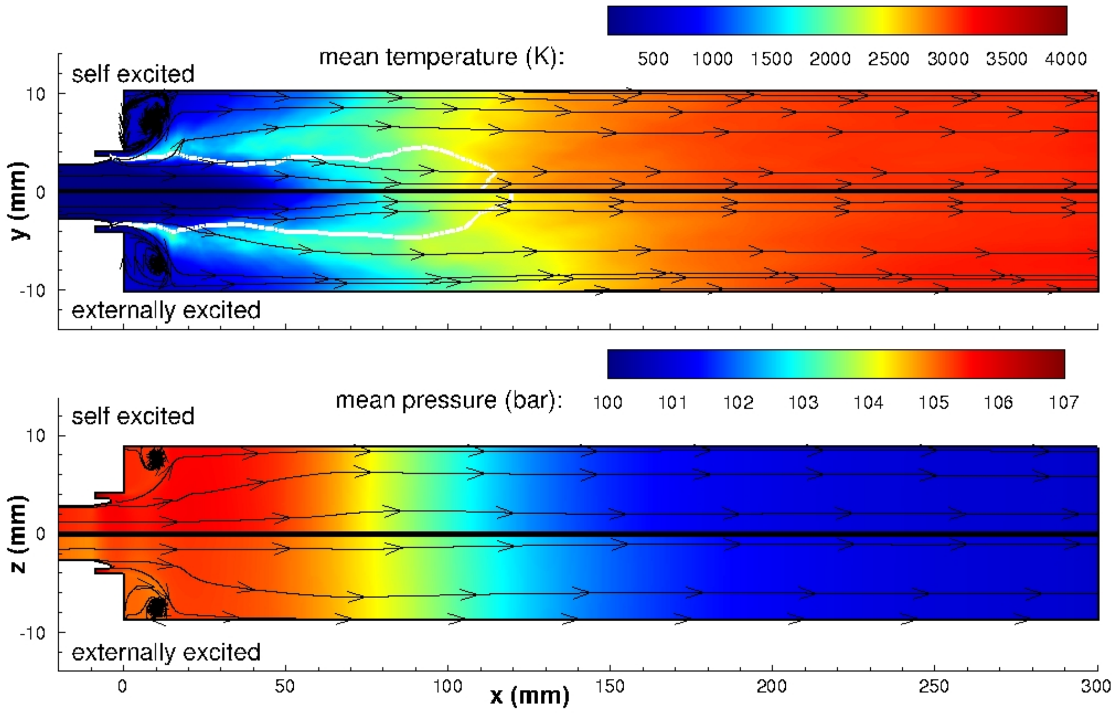

Figure 4: Mean temperature distributions in the $z = 0$ mm plane including mean stoichiometric mixture fraction as white line (top) and pressure distributions in the $y = 0$ mm plane (bottom) for both operation points. Streamtraces indicate the recirculation zones at the face plate. X-axis compressed by a factor of 3.

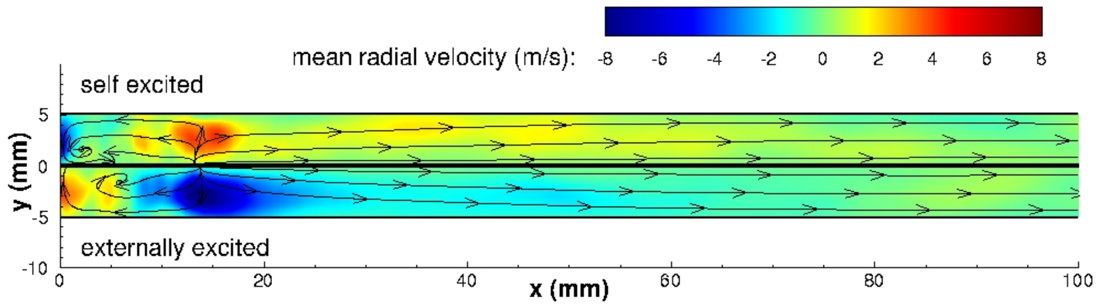

Figure 5: Mean radial velocity distribution in the $z = 8.8$ mm-plane (boundary of the domain). Stream traces indicate recirculation towards the corner points of the hexagonal cross section.

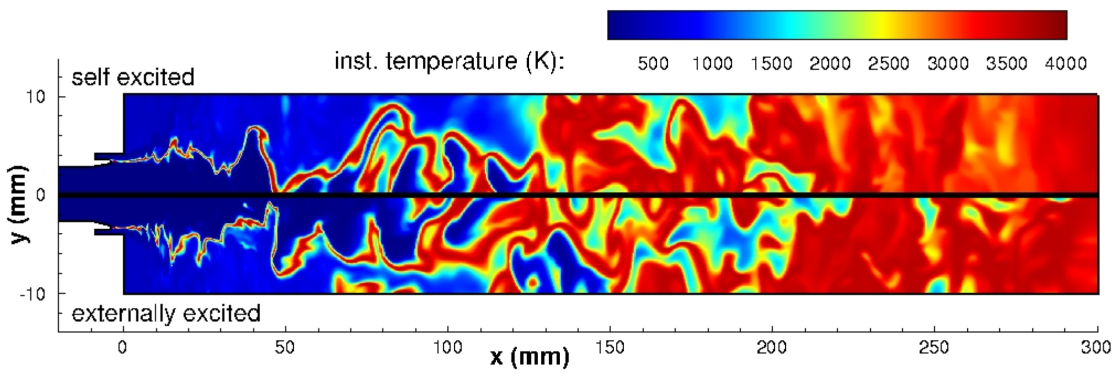

Figure 6: Instantaneous temperature distribution in the $z = 0$ mm plane. X axis compressed by a factor of 3.

DOI: 10.13009/EUCASS2022-6075

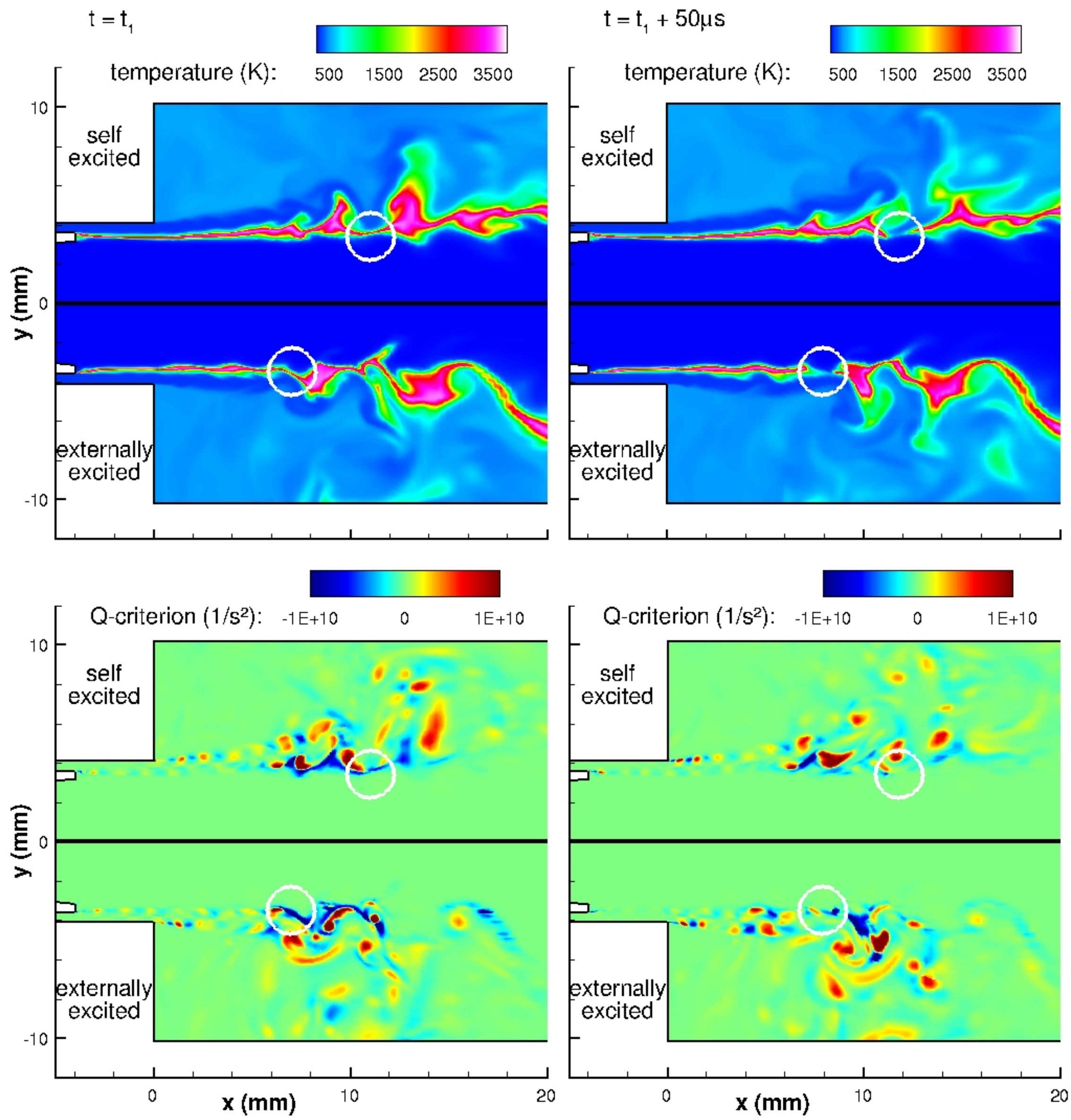

Figure 7: Instantaneous temperature distributions (top) and Q-criterion distributions (bottom) for both operation points in the $z = 0$ mm plane. Time is advanced from left to right by 50 µs. White circles highlight the process of flame extinction.

Generally, standing waves with two open ends arise within rocket combustion chambers, where the frequency of the N-th mode can be determined by

$$f_N^L = \frac{a}{\lambda_N} \,, \tag{14}$$

$$\text{with} \quad \lambda_N = \frac{2}{N} L_{eff} \,, \tag{15}$$

where a is the mean speed of sound and λ_N the wave length of the mode. The rear end of the standing wave is usually located between nozzle entry and nozzle throat and the effective length L_{eff} of the resonator is the distance between face plate and this point.

In the given test case the nozzle is neglected and the mean combustion chamber pressure is prescribed by a subsonic outflow boundary condition. Although a non-reflective boundary condition is used, some information, i.e. the pressure at infinity, must enter the combustor from outside the domain. This is not the case with perfect non-reflective boundary conditions, which, however, result in an underdetermined set of equations and pressure drift.[37] In order to avoid this, the outflow here is partly reflective. In this way the chamber pressure is kept close to 100 bar with a mean

DOI: 10.13009/EUCASS2022-6075

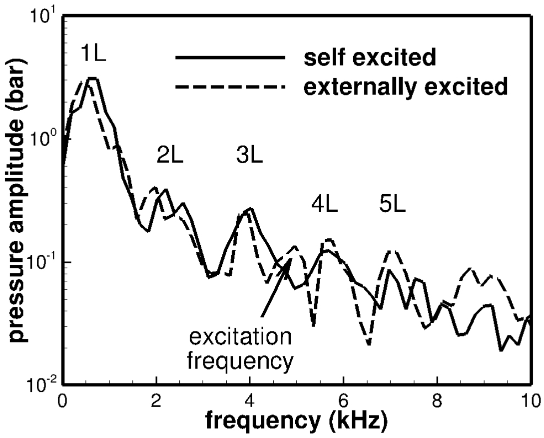

Figure 8: Frequency spectra of the self excited and the externally excited test case. Monitor points at $x = y = z = 0$ mm.

Table 2: Frequencies of the longitudinal modes of the self-excited operation point and the effective resonator length assuming the speed of sound to be 1050 m/s.

mode	simulated frequency (kHz)	effective resonator length (mm)
1	0.65	400
2	2.20	360
3	4.00	330
4	5.60	330
5	7.05	340

error of 1 %. A side effect of this method is, that the standing waves inside this combustion chamber have a closed rear end or pressure node. Hence, the equation for the wavelengths changes to

$$\lambda_N = \frac{4}{2N-1} L_{eff} \,. \tag{16}$$

Because the pressure can oscillate at the rear edge of the domain due to the partly reflective outflow boundary condition, the pressure node is somewhat downstream of the exit plane. Thus, L_{eff} is expected to be slightly longer than the considered combustion chamber length.

The frequency spectra for both operation points are given in Fig. 8. The monitor point is located on the main axis directly at the combustion chamber entry ($x = y = z = 0$ mm). Similar to the mean and instantaneous flow fields, there are only minor deviations between the two cases. In Tab. 2 the frequencies of the first five longitudinal modes are given for the self excited operation point. For this simulation, the time and space averaged speed of sound in the combustor is approximately 1050 m/s. Using Eq. (14) and (16) the effective resonator lengths can be estimated, which are also given in Tab. 2. The frequency of the first longitudinal mode is 0.65 kHz. This is only half the frequency that would occur in this combustor, if the outflow nozzle would be included in the simulation. It should be mentioned, that the frequency resolution of the FFT is about $\Delta f = 0.2$ kHz with the consequence, that the error in the first longitudinal mode can be large. For a better resolution the simulation has to be carried out over a longer period of time. Overall, the effective resonator length is about 10 to 20 % longer than the simulation domain and thus within the expected range.

For the externally exited test case, the excitation frequency is hardly noticeable at the entry of the combustion chamber (Fig. 8 at 5 kHz). Because the excitation does not match a resonant frequency of the combustor, the mode is strongly damped. The amplitude of the excitation is reduced by almost two orders of magnitude from 10 bar at the inflow boundary to 0.14 bar at the combustion chamber entry. Hence, the influence of excitation inside the combustion chamber is limited. This is in agreement with the minor differences between the cases with and without excitation observed in the flow fields.

DOI: 10.13009/EUCASS2022-6075

Table 3: Volume fraction of different flame regimes for a single time step in the defined domains.

domain	mostly diffusive ($FI <= 0$) in %	mostly premixed ($FI > 0$) in %
$x < 7$ mm	74.17	25.83
7 mm $< x <$ 60 mm	51.82	48.18
60 mm $< x <$ 200 mm	54.05	45.95
$x > 200$ mm	91.59	8.41

4.3 High pressure methane / oxygen combustion

In this section the methane chemistry is investigated in detail. Therefore, the combustion is divided by the flame index[35]

$$FI = \langle \nabla Y_{O_2}, \nabla Y_{CH_4} \rangle \tag{17}$$

into mostly premixed ($FI > 0$) and mostly diffusive ($FI \leq 0$) combustion regimes. In addition, the combustion chamber can be divided into four sections with respect to the axial direction which are dominated by different flow and flame effects. The four domains and the volume fraction of the different flame regimes are summarized in Tab. 3 for a single time step. Corresponding scatter plots for the temperature (Fig. 9) and several species mass fractions (Figs. 10 and 11) depending on the mixture fraction show for the same time step the flame characteristics in more detail. Thereby, each point corresponds to one cell of the domain and is colorized by the Frobenius norm of the strain rate tensor

$$||\boldsymbol{S}|| = \sqrt{\sum_{i=1}^{3}\sum_{j=1}^{3}|s_{ij}|}\,, \quad \text{with} \quad \boldsymbol{S} = \nabla\vec{u}\ , \tag{18}$$

where $\vec{u}$ denotes the velocity vector.

In the first domain ($x < 7$ mm) the flame is smooth and stable. As depicted in the upper left part of Fig. 9, for $\xi < 0.3$ (lean or close to stoichiometry) the flow is close to chemical equilibrium. For higher mixture fractions the chemical processes are in good agreement with a flamelet line with a mean strain rate of $S = 1900\,1/\mathrm{s}$. Similar deviations from chemical equilibrium are found by Gerlinger[9] for the hydrogen driven PennState model rocket combustor using a transported Probability Density Function (tPDF) method. The flamelet curve is calculated with Cantera[12] using a one dimensional couterflow diffusion model. Further, the flame is mostly in diffusive regime, but a significant amount of the lean zones are in premixed regime (Fig. 10, top row). Moreover, the LOx core is still intact.

As already mentioned in Sec. 4.1 the second part of the combustor (7 mm $< x <$ 60 mm) is dominated by growing shear layer instabilities which causes flame extinction, which occurs only in this domain. This can be clearly seen in the upper right scatter plot of Fig. 9. Here, the temperature in a large number of volumes is much lower than chemical equilibrium would suggest. Moreover, Fig. 10 shows that significant parts of the fuel rich flame are now found in the premixed regime. Combined, these characteristics have a strong impact on flame stabilization and flame length.

In the third domain which extends from $x = 60$ to 200 mm the flame burns stable again and the combustion approaches chemical equilibrium (Fig. 9, bottom left and Fig. 10, third row). Moreover, the number of volumes in premixed regime decreases. This results in a mainly diffusive flame in the last third of the combustion chamber (Fig. 10, last row). Here, combustion chemistry is mostly close to chemical equilibrium, which is shown by the bottom right scatter plot of Fig. 9. Finally, in the fourth domain of the combustor the combustion is basically completed.

Fig. 11 depicts scatter plots of additional species mass fractions over mixture fraction separated in the second domain where flame extinction takes place and all other domains. Generally, the agreement of the influence of the strain rate calculated by the finite-rate LES and the corresponding flamelet curves is quite good for the flow without extinction. The strongly increased values of CH_3 and reduced values of CO can be reproduced by both methods. In region 2 where flame extinction takes place the differences between the finite-rate LES and the flamelet curves are considerably larger, especially for carbon dioxide. Nevertheless, the tendencies are matching here, too. Furthermore, Fig. 11 shows, that for lean mixture the combustion chemistry is close to chemical equilibrium. In contrast, for fuel rich conditions the influence of strain increases.

DOI: 10.13009/EUCASS2022-6075

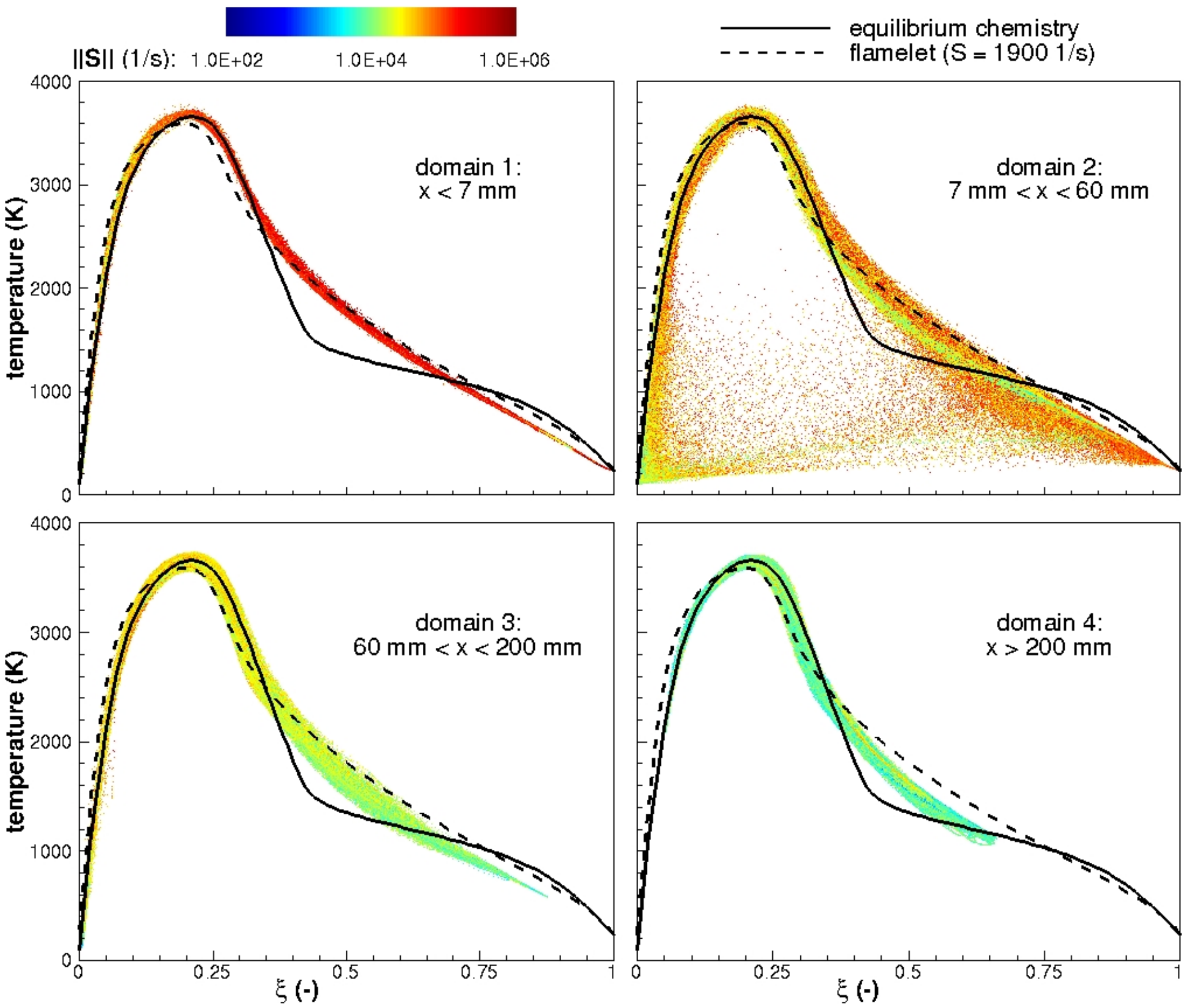

Figure 9: Scatter plot of the temperature in four different domains inside the combustor against the mixture fraction. Colorized by the magnitude of the strain rate tensor. Flamelet curve and equilibrium chemistry as reference.

5. Conclusion

In this paper, a numerical investigation of a methane-oxygen rocket combustion chamber with transcritical injection is presented. The time accurate simulations were carried out with the in-house code TASCOM3D on structured grids using the hybrid iDDES method with a 5th order spatial discretization scheme and detailed chemistry. By the use of periodic boundary conditions instead of combustion chamber walls, a virtual multi-injector combustor is modeled. Furthermore, the nozzle is neglected and the mean chamber pressure is prescribed by a subsonic weakly reflecting outflow boundary condition.

Two different test cases were simulated with the same mean inflow conditions, one featuring a sinusoidally excited oxidizer inflow. It is shown, that only small deviations in mean flow field result from the excitation. A dynamic pressure analysis confirms, that the externally excitation does not match a resonant frequency of the combustor. Thus, the mode is already damped by about two orders of magnitude until entering the combustion chamber. It can be concluded that high frequency oscillations (in this case 5 kHz) in the supply system with moderate amplitudes do not significantly effect the combustion processes. Further, the analysis of the dynamic pressure modes of this comubstor shows that occurring longitudinal modes have a pressure node at the rear end due to the prescribed outlet pressure. This is in contrast to simulations including the nozzle in which both ends of the longitudinal modes are open ends. Thus, the dynamic behavior changes significantly by neglecting the nozzle. Hence, it is of importance for the simulation of rocket engines to consider the nozzle, what requires compressible flow solvers.

Although high pressures accelerate the combustion kinetics, investigations of the chemical processes showed, that the combustion of methane with oxygen is in large parts of the combustor far from chemical equilibrium especially

DOI: 10.13009/EUCASS2022-6075

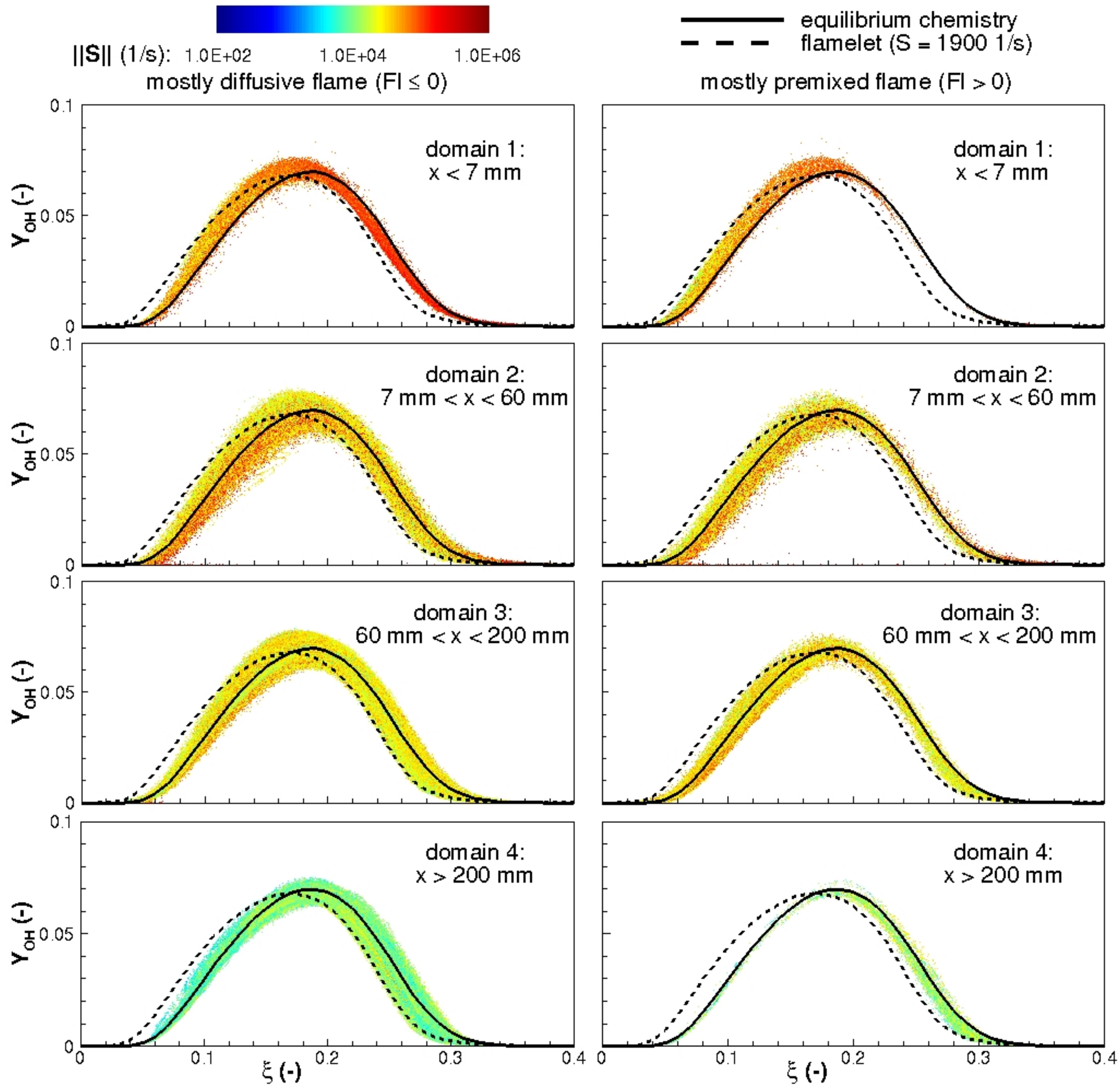

Figure 10: Scatter plots of the OH mass fraction in the four different domains of the combustor (top to bottom). Separated in the diffusive (left) and premixed region (right). Flamelet curve and equilibrium chemistry as reference.

in fuel rich regions. Moreover, flame extinction takes place which is caused by shear layer instabilities. This has a strong impact on the mean flame length. The combination of iDDES and finite-rate chemistry demonstrates their ability to reproduce these processes, which justifies the high computational cost.

6. Acknowledgments

The present work was conducted in the framework of the German Aerospace Center project **A**dvanced **M**ethods for Reusable **A**erospace Vehicle **DE**sign **U**sing Artificial Intelligence and Interdisciplinary Numerical **S**imulation (AMADEUS) focusing on the qualification and advancement of the German Aerospace Center (DLR) flow solver TAU for liquid rocket thrust chamber applications. The financial support of the DLR Space Research Programmatic is highly appreciated.

All simulations were performed on the HPE Apollo cluster Hawk at the High-Performance Computing Center Stuttgart (HLRS) under the grant number scrcomb. The authors wish to thank for the computing time and the technical support.

DOI: 10.13009/EUCASS2022-6075

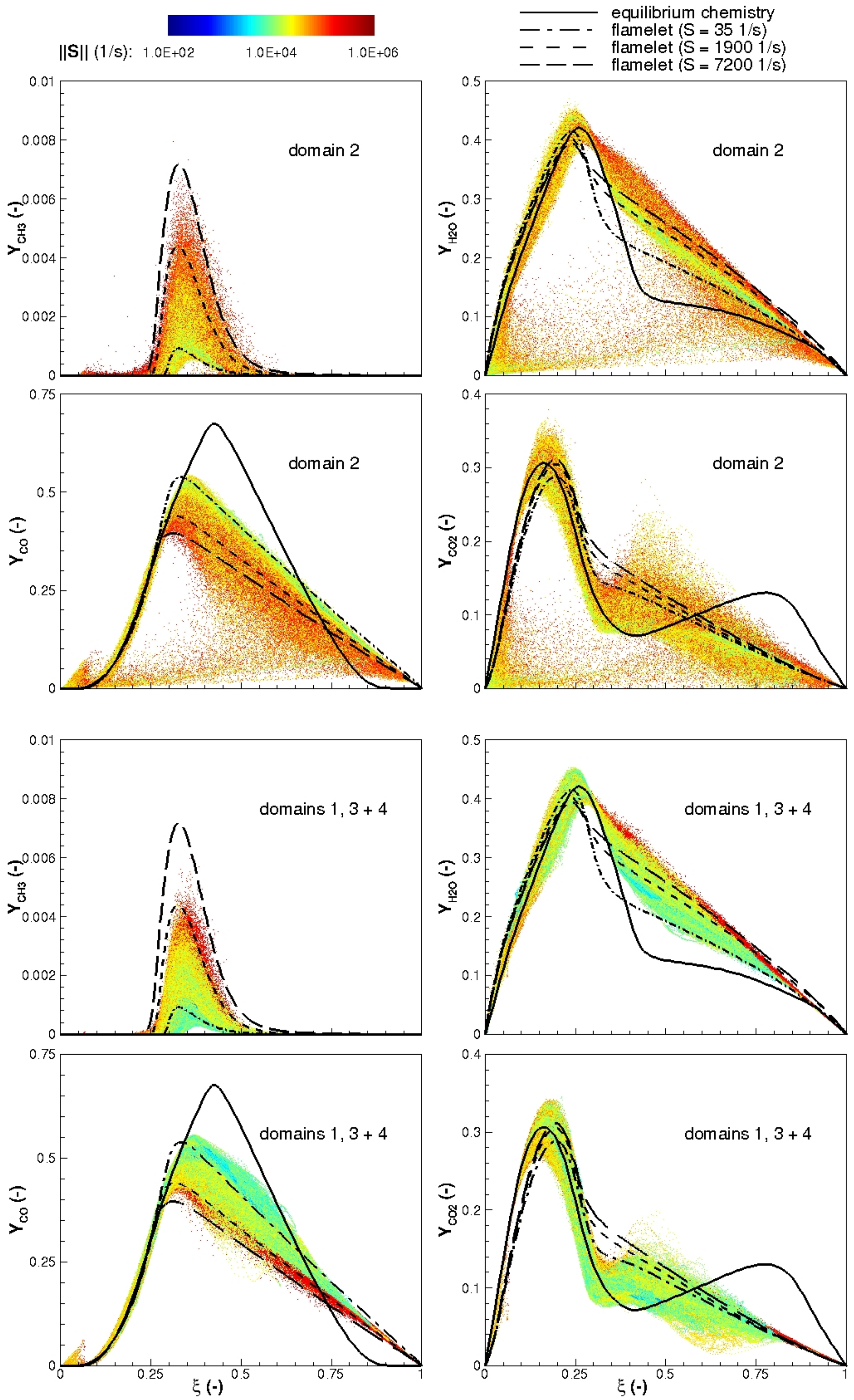

Figure 11: Scatter plots of different species mass fraction against mixture fraction separated into regions with (top) and without flame extinction (bottom). Flamelet curves and equilibrium chemistry as reference.

DOI: 10.13009/EUCASS2022-6075

References

[1] Robert A. Baurle, G. A. Alexopoulos, and Hazhar A. Hassan. Assumed joint probability density function approach for supersonic turbulent combustion. *Journal of Propulsion and Power*, 10(4):473–484, jul 1994.

[2] Lawrence J. De Chant. The venerable 1/7th power law turbulent velocity profile: a classical nonlinear boundary value problem solution and its relationship to stochastic processes. *Applied Mathematics and Computation*, 161(2):463–474, feb 2005.

[3] Lars Davidson. Large Eddy Simulations: How to evaluate resolution. *International Journal of Heat and Fluid Flow*, 30(5):1016–1025, oct 2009.

[4] Jochen Frölich. *Large-Eddy-Simulation turbulenter Strömungen*. Teubner, Wiesbaden, 2006.

[5] Charles William Gear. *Numerical Initial Value Problems in Ordinary Differential Equations*. Prentice Hall, 1971.

[6] P. Gerlinger, K. Nold, and M. Aigner. Influence of reaction mechanisms, grid spacing, and inflow conditions on the numerical simulation of lifted supersonic flames. *International Journal for Numerical Methods in Fluids*, pages n/a–n/a, 2009.

[7] Peter Gerlinger. *Numerische Verbrennungssimulation*. Springer Berlin Heidelberg, 2005.

[8] Peter Gerlinger. Multi-dimensional limiting for high-order schemes including turbulence and combustion. *Journal of Computational Physics*, 231(5):2199–2228, mar 2012.

[9] Peter Gerlinger. Lagrangian transported mdf methods for compressible high speed flows. *Journal of Computational Physics*, 339:68–95, 2017.

[10] Peter Gerlinger, Berthold Noll, and Manfred Aigner. Assumed pdf modelling and pdf structure investigation using finite-rate chemistry. *Progress in Computational Fluid Dynamics, An International Journal*, 5(6):334–344, 2005.

[11] Sharath Girimaji. A simple recipe for modeling reaction-rate in flows with turbulent-combustion. In *22nd Fluid Dynamics, Plasma Dynamics and Lasers Conference*. American Institute of Aeronautics and Astronautics, jun 1991.

[12] Dave G. Goodwin, Harry K. Moffat, Ingmar Schoegl, Taymond L. Speth, and Bryan W. Weber. Cantera: An Object-oriented Software Toolkit for Chemical Kinetics, Thermodynamics and Transport Processes. `https://www.cantera.org/`, 2022. Version 2.5.1.

[13] Jinhee Jeong and Fazle Hussain. On the identification of a vortex. *Journal of fluid mechanics*, 285:69–94, 1995.

[14] Roman Keller and Peter M. Gerlinger. Numerical Simulations of a Single Injector Gaseous Methane Rocket Combustion Chamber. In *54th AIAA Aerospace Sciences Meeting*. American Institute of Aeronautics and Astronautics, jan 2016.

[15] Markus Kindler. *Verbrennungssimulation in instationären kompressiblen Strömungen*. PhD thesis, Universität Stuttgart, 2014.

[16] K. J. Laidler. A glossary of terms used in chemical kinetics, including reaction dynamics (IUPAC Recommendations 1996). *Pure and Applied Chemistry*, 68(1):149–192, jan 1996.

[17] Ansgar Lechtenberg and Peter Gerlinger. Numerical investigation of combustion instabilities in a rocket combustion chamber with supercritical injection using a hybrid rans/les method. In *AIAA Scitech 2020 Forum*. American Institute of Aeronautics and Astronautics, 2020.

[18] Markus Lempke, Peter Gerlinger, Martin J. Seidl, and Manfred Aigner. Unsteady high-order simulation of a liquid oxygen/gaseous hydrogen rocket combustor. *Journal of Propulsion and Power*, 31(6):1715–1726, nov 2015.

[19] Meng-Sing Liou. On a new class of flux splitting. In *Thirteenth International Conference on Numerical Methods in Fluid Dynamics*, pages 115–119. Springer, 1993.

[20] Stephen B Pope. *Turbulent flows*. Cambridge university press, 2000.

DOI: 10.13009/EUCASS2022-6075

[21] Thomas Schmitt, Laurent Selle, Bénédicte Cuenot, and Thierry Poinsot. Large-eddy simulation of transcritical flows. *Comptes Rendus Mécanique*, 337(6-7):528–538, jun 2009.

[22] Martin Seidl. *Numerische Simulation von Raketenbrennkammern mit transkritischer Einspritzung*. PhD thesis, Universität Stuttgart, 2018.

[23] Martin J. Seidl, Manfred Aigner, Roman Keller, and Peter Gerlinger. CFD simulations of turbulent nonreacting and reacting flows for rocket engine applications. *The Journal of Supercritical Fluids*, 121:63–77, mar 2017.

[24] Timo Seitz and Peter Gerlinger. Comparison of hybrid rans/les models for rocket combustion chamber simulations. In *AIAA Scitech 2021 Forum*, page 1543, 2021.

[25] Eiji Shima and Keiichi Kitamura. Parameter-free simple low-dissipation AUSM-family scheme for all speeds. *AIAA Journal*, 49(8):1693–1709, aug 2011.

[26] Jian-Shun Shuen. Upwind differencing and lu factorization for chemical non-equilibrium navier-stokes equations. *Journal of Computational Physics*, 99(2):233–250, 1992.

[27] Jian Shun Shuen and Seokkwan Yoon. Numerical study of chemically reacting flows using a lower-upper symmetric successive overrelaxation scheme. *AIAA journal*, 27(12):1752–1760, 1989.

[28] Mikhail L Shur, Philippe R Spalart, Mikhail Kh Strelets, and Andrey K Travin. A hybrid RANS-LES approach with delayed-DES and wall-modelled LES capabilities. *International Journal of Heat and Fluid Flow*, 29(6):1638–1649, 2008.

[29] Yann Hendrik Simsont and Peter Gerlinger. High Order Numerical Simulation of the Thermal Load on a Lobed Strut Injector for Scramjet Applications. *International Journal for Numerical Methods in Fluids*, 82(7):417–436, feb 2016.

[30] Giorgio Soave. Equilibrium constants from a modified Redlich-Kwong equation of state. *Chemical Engineering Science*, 27:1197–1203, 1972.

[31] Geoffrey Ingram Taylor. The spectrum of turbulence. *Proceedings of the Royal Society of London. Series A - Mathematical and Physical Sciences*, 164(919):476–490, 1938.

[32] Christoph Traxinger, Julian Zips, and Michael Pfitzner. Large-eddy simulation of a multi-element LOx/CH_4 thrust chamber demonstrator of a liquid rocket engine. In *8th European Conference for Aeronautics and Space Sciences (EUCASS). Madrid, Spain*, 2019.

[33] Jürgen Warnatz, Ulrich Maas, Robert W. Dibble, and U. Maas. *Verbrennung*. Springer-Verlag GmbH, 2001.

[34] David C. Wilcox. Formulation of the k-ω Turbulence Model Revisited. *AIAA Journal*, 46(11):2823–2838, nov 2008.

[35] H. Yamashita, M. Shimada, and T. Takeno. A numerical study on flame stability at the transition point of jet diffusion flames. *Symposium (International) on Combustion*, 26(1):27–34, jan 1996.

[36] Vigor Yang. Liquid-propellant rocket engine injector dynamics and combustion processes at supercritical conditions. Technical report, Pennsylvania State University Park Dept of Mechanical Engineering, 2004.

[37] Chun Sang Yoo and Hong G Im. Characteristic boundary conditions for simulations of compressible reacting flows with multi-dimensional, viscous and reaction effects. *Combustion Theory and Modelling*, 11(2):259–286, 2006.